Regular Article – Experimental Physics

Beta-delayed proton emission from ^{20}Mg

IDS Collaboration

M.V. Lund[1,a], A. Andreyev[2], M.J.G. Borge[3,4], J. Cederkäll[5], H. De Witte[6], L.M. Fraile[7], H.O.U. Fynbo[1], P.T. Greenlees[8,9], L.J. Harkness-Brennan[10], A.M. Howard[1], M. Huyse[6], B. Jonson[11], D.S. Judson[10], O.S. Kirsebom[1], J. Konki[8,9], J. Kurcewicz[4], I. Lazarus[12], R. Lica[4,13], S. Lindberg[11], M. Madurga[4], N. Marginean[13], R. Marginean[13], I. Marroquin[3], C. Mihai[13], M. Munch[1], E. Nacher[3], A. Negret[13], T. Nilsson[11], R.D. Page[10], S. Pascu[13], A. Perea[3], V. Pucknell[12], P. Rahkila[8,9], E. Rapisarda[4], K. Riisager[1], F. Rotaru[13], C. Sotty[6,13], M. Stanoiu[13], O. Tengblad[3], A. Turturica[13], P. Van Duppen[6], V. Vedia[7], R. Wadsworth[2], and N. Warr[14]

1   Department of Physics and Astronomy, Aarhus University, DK-8000 Aarhus C, Denmark
2   University of York, Department of Physics, York YO10 5DD, N Yorkshire, UK
3   Instituto de Estructura de la Materia, CSIC, E-28006 Madrid, Spain
4   ISOLDE, PH Department, CERN, CH-1211 Geneva 23, Switzerland
5   Department of Nuclear Physics, Lund University, SE-221 00 Lund, Sweden
6   KU-Leuven, Instituut voor Kern- en Stralingsfysica, Celestijnenlaan 200D, B-3001 Leuven, Belgium
7   Facultad de Ciencias Fisicas, Universidad Complutense de Madrid, CEI Moncloa, 28040 Madrid, Spain
8   Helsinki Institute of Physics, University of Helsinki, P.O. Box 64, FIN-00014 Helsinki, Finland
9   University of Jyväskylä, Department of Physics, P.O. Box 35, FIN-40014 University of Jyväskylä, Jyväskylä, Finland
10 Department of Physics, Oliver Lodge Laboratory, University of Liverpool, Liverpool L69 7ZE, UK
11 Department of Physics, Chalmers University of Technology, SE-412 96 Göteborg, Sweden
12 STFC Daresbury, Daresbury, Warrington WA4 4AD, UK
13 "Horia Hulubei" National Institute of Physics and Nuclear Engineering, RO-077125 Magurele, Romania
14 Institut für Kernphysik, Universität zu Köln, Zülpicher Strasse 77, D-50937 Köln, Germany

Abstract. Beta-delayed proton emission from ^{20}Mg has been measured at ISOLDE, CERN, with the ISOLDE Decay Station (IDS) setup including both charged-particle and gamma-ray detection capabilities. A total of 27 delayed proton branches were measured including seven so far unobserved. An updated decay scheme, including three new resonances above the proton separation energy in ^{20}Na and more precise resonance energies, is presented. Beta-decay feeding to two resonances above the Isobaric Analogue State (IAS) in ^{20}Na is observed. This may allow studies of the 4032.9(2.4) keV resonance in ^{19}Ne through the beta decay of ^{20}Mg, which is important for the astrophysically relevant reaction ^{15}O$(\alpha, \gamma)^{19}$Ne. Beta-delayed protons were used to obtain a more precise value for the half-life of ^{20}Mg, 91.4(1.0) ms.

1 Introduction

^{20}Mg is located on the proton drip line with a half-life of 90(6) ms according to the latest evaluation [1]. It beta decays by allowed transitions to excited states in ^{20}Na with $I^\pi = 0^+, 1^+$ as the ground state of ^{20}Mg is a 0^+ state. Due to the large beta-decay energy of drip-line nuclei in general, they are a source of many different decay channels [2–4], and ^{20}Mg is no exception. It has several energetically allowed decay channels: $\beta\gamma$, βp, $\beta\alpha$, $\beta p\alpha$ and $\beta\alpha p$. Only the first two have been observed previously [5–8]. The present understanding of the decay of ^{20}Mg is mainly based on refs. [5] and [7]. The most recent result

on ^{20}Mg [8] is the accurate and precise determination of the excitation energy of the IAS in ^{20}Na, 6498.4(5) keV, which revalidates the Isobaric Multiplet Mass Equation (IMME) for the $A = 20$ quintet by shifting its excitation energy down by 27 keV.

The main ^{20}Mg beta branch feeds the 984 keV state of ^{20}Na ($I_\beta = 69.7(1.2)\%$ [5]), which is located below the proton separation energy, $S_p = 2190.1(1.1)$ keV [6]. This state decays to the ground state of ^{20}Na by emission of a single gamma ray. It is followed by the beta decay of ^{20}Na to ^{20}Ne, which has a substantial decay branch of beta-delayed alpha-particle emission (19.95(34)% based on ref. [9] pp. 313, 314) that results in low-energy ^{16}O recoils. These pose a challenge when interpreting the low-energy part of the beta-delayed proton spectrum from

a   e-mail: morten.vinther.lund@gmail.com

^{20}Mg, as the detection system does not allow discrimination between the low-energy protons and the ^{16}O recoils.

The beta-delayed proton emission from ^{20}Mg feeds resonances in ^{19}Ne. The ground state of ^{19}Ne (plus proton mass) is located 2190.1(1.1) keV [6] above the ground state of ^{20}Na and the known excited states are located at 238.27(11) keV, 275.09(13) keV, 1507.56(30) keV, 1536.0(4) keV, 1615.6(5) keV, 2794.7(6) keV, and 4032.9(2.4) keV [10]. The four lowest excited states are known to be populated by the beta decay of ^{20}Mg. However, the small energy gap (37 and 28 keV) between them presents an experimental challenge when measuring the beta-delayed proton spectrum. The measurement of the individual decay branches becomes easier if the protons are measured in coincidence with the gamma rays de-exciting the states. The first and second excited states can only decay to the ground state by emission of a single gamma ray. The third and fourth excited states decay predominantly to the second ($I_{\gamma,\mathrm{3rd}\to\mathrm{2nd}} = 88\%$ [10]) and first ($I_{\gamma,\mathrm{4th}\to\mathrm{1st}} = 95\%$ [10]) excited state, respectively. They do, however, have a small branch to the first ($I_{\gamma,\mathrm{3rd}\to\mathrm{1st}} = 12\%$ [10]) and second ($I_{\gamma,\mathrm{4th}\to\mathrm{2nd}} = 5\%$ [10]) excited state, respectively.

At an excitation energy of 4032.9(2.4) keV the seventh excited state in ^{19}Ne is located in the Gamow window of the ^{15}O$(\alpha,\gamma)^{19}$Ne reaction. This is the first reaction in the first breakout sequence from the HCNO-cycles [11] with the second reaction being ^{19}Ne(p, $\gamma)^{20}$Na. The breakout sequence is leaking C, N and O seed nuclei into the $A > 20$ region and it is followed by the αp- and the rp-processes. The 4032.9(2.4) keV resonance is dominating the ^{15}O(α,γ) reaction rate under type I X-ray burst conditions [12]. To quantify the reaction rate it is important to measure the alpha-particle emission branching ratio of the 4032.9(2.4) keV resonance. It is expected to be roughly 10^{-4} [13,14], but it has never been measured directly as the Coulomb barrier suppresses the rate of alpha-particle emission. The beta decay of ^{20}Mg has a large enough Q_{EC}-value to feed the resonance through beta-delayed proton emission, so it should be possible with enough statistics to observe $\beta p\alpha$ as well as $\beta p\gamma$ emission through this resonance.

The 2647(3) keV resonance in ^{20}Na is located just above the threshold for proton emission, $S_p = 2190.1(1.1)$ keV [6]. It is the most important resonance for determining the ^{19}Ne(p, $\gamma)^{20}$Na reaction rate in X-ray bursters, as it is located in the Gamow window of the reaction. The spin and parity of this resonance have been the subject of some debate in the past. The present understanding point towards $I^\pi = 3^+$ [7], however, a 1^+ assignment is not yet fully ruled out. On the basis of the beta-decay feeding of this resonance, it is possible to set stringent limits on the spin and parity when considering the selection rules for an allowed beta decay.

This paper presents the results of a beta-decay study of ^{20}Mg performed at the ISOLDE Decay Station (IDS). A detailed description of the experiment, analysis and results can be found in ref. [15]. In this paper, we will start by describing the beam production, the experimental setup and the calibration procedures in sect. 2. In sect. 3 we will present the measured particle spectra and a determination of the half-life. Then we will explain the reconstruction of the decay scheme and the determination of the absolute beta-decay intensities in sect. 4. At the end of sect. 4, we will also present and discuss the status of the astrophysically relevant states.

2 Experimental methods

2.1 Beam production

The beam of ^{20}Mg was produced at the ISOLDE facility [16] at CERN by bombarding a SiC target with a pulsed 1.4 GeV proton beam from the Proton-Synchrotron Booster (PSB). The magnesium nuclei were selectively ionized with the laser-ion source RILIS [17]. However, a large amount of sodium was also ionized due to surface ionization. The cocktail beam was accelerated to 30 keV and mass separated with the High Resolution Separator (HRS), $M/\Delta M = 5000$, with a slit cutting away part of the beam on the low-mass side (^{20}Na). To further suppress the isobaric contamination of sodium, we made use of the PSB time structure of 1.2 s separated proton pulses (each proton pulse has a width of 1.7 ms). Taking advantage of the fact that the time for magnesium ions to diffuse out of the target, be ionized and transported to the detection chamber is of the order of 150 ms, and that the half-lives differ significantly for ^{20}Mg ($T_{1/2} = 90(6)$ ms [1]) and ^{20}Na ($T_{1/2} = 447.9(2.3)$ ms [1]), we only allow the beam into the detection chamber for the first 300 ms following proton impact on the production target.

The mass separated beam was implanted in a carbon foil of thickness 24.5(5) μg/cm^2 in the center of the detection setup, see fig. 1. The thickness of the carbon foil was determined by measuring the energy loss of alpha particles from a known source as they passed through the carbon foil. From measurements of the decay of ^{20}Mg and ^{20}Na we estimate that for every ^{20}Mg ion implanted, we implanted about 23 ^{20}Na ions in the carbon foil. By counting all decay products from the beta decay of ^{20}Mg, we determine the total number of implanted ^{20}Mg ions to be $7.64(16) \cdot 10^6$. The total measurement time was 53.2 hrs.

Initially we experienced problems with beam losses on a collimator at the entrance to the detection chamber. We optimized the beam tuning parameters and obtained an almost complete transfer into the detection chamber. However, from analysis of the ^{20}Na beta decay we suspect that a fraction of the beam is implanted in the collimator (not shown in fig. 1), which leads to a small systematic error when determining the branching ratios. This is discussed in detail in sect. 4.3.

2.2 Detection setup

The detection setup is shown in fig. 1. It is the IDS charged-particle spectroscopy setup, which consists of a silicon detector array (nos. 1–5) in close geometry of the
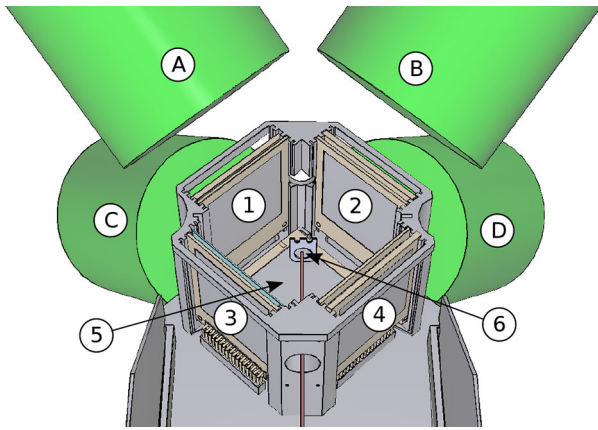
Fig. 1. (Color online) Sketch of detector setup. The beam is coming from the bottom of the figure and is implanted in the carbon foil in the center of the setup (no. 6). Surrounding the foil are four charged-particle telescopes (nos. 1–4) and below the foil is a single thick DSSSD (no. 5). Outside the vacuum chamber (not shown here) are the four HPGe clover detectors (A–D). We will refer to this numbering throughout the paper.

carbon foil (no. 6) in which the beam is implanted. The beam is stopped at the center of the carbon foil. Surrounding the silicon detector array we placed four clover HPGe detectors (A–D). The detector setup is therefore able to detect both charged particles and gamma rays with high efficiency.

The silicon detector array consisted of four ΔE-E telescopes forming the sides of a cube (nos. 1–4) enclosing the carbon foil (no. 6) and one $1000\,\mu m$ thick Double Sided Silicon Strip Detector (DSSSD, no. 5) forming the bottom of the cube. The top of the cube was left open in order to allow room for the carbon foil support. The four telescopes were in the following configurations: $20\,\mu m$ SSD (Single-sided Strip Detector, 16 front strips) - $500\,\mu m$ DSSSD (no. 3), $40\,\mu m$ DSSSD - $500\,\mu m$ pad (no. 4), $60\,\mu m$ DSSSD - $500\,\mu m$ pad (no. 1), and $300\,\mu m$ DSSSD - $500\,\mu m$ pad (no. 2). Each of the backing detectors covered a solid angle of about 4.7% out of 4π, while the front detectors each covered a solid angle of about 5.2% of 4π. All of the DSSSDs were 16×16 strip detectors with $3.0\,mm$ strip width and $0.1\,mm$ interstrip width.

The silicon detector setup was designed to maximize the solid-angle coverage. To produce clean proton spectra we used thin front detectors in three of the four telescopes. The alpha particles from the decay of ^{20}Na will then be stopped in the front detector, while the protons will punch through the front detector due to their lower stopping power. For the $40\,\mu m$ and $60\,\mu m$ silicon detectors all the alpha particles will be stopped, whereas for the $20\,\mu m$ detector the most energetic alpha particles will punch through. In the fourth telescope we placed a $300\,\mu m$ thick front detector in order to obtain a better energy resolution than the thinner detectors. The backing detectors were chosen to be $500\,\mu m$ thick in order to stop all protons. On all five sides of the detector array we used one 16×16 strip DSSSD in order to be position sensitive. The silicon detectors were placed in a 3D-printed support structure

such that the telescopes pairwise faced each other, in order to be able to make coincidence gates as efficient as possible.

Data from the HPGe detectors were recorded simultaneously with a digital and an analog data acquisition (daq) system. While the digital daq has superior energy resolution (see sect. 2.4), only the analog system was recording charged-particle events, which allows one to study particle-gamma coincidences. All HPGe-detector crystals were treated as individual detectors in the analysis of the data from the analog daq system.

2.3 Silicon detector calibration

For the geometry and energy calibrations of the silicon detector setup, we used a beam of ^{21}Mg. The ^{21}Mg ions were produced in the same manner as the ^{20}Mg ions. Due to the similar masses both beams will stop at the same depth in the carbon foil to within $1\,nm$ (estimate based on stopping powers). The beta decay of ^{21}Mg is well known, see *e.g.* [18–20], and it exhibits several high-intensity βp transitions, which we have used for the calibration. However, for the very thin front detectors of $20\,\mu m$ and $40\,\mu m$ most proton lines punch through the detector. For these detectors we have used the well-known beta-delayed alpha lines from ^{20}Na.

For the unsegmented pad detectors positioned as backing detectors in three of the four telescopes, we used the ^{21}Mg decay as a calibration source. However, in the case of telescope no. 2 the front detector is $300\,\mu m$ thick, and the protons do not reach the pad detector. Hence we have used measurements with a quadruple alpha source (^{148}Gd, ^{239}Pu, ^{241}Am and ^{244}Cm) for the calibration of this detector.

For all energy calibrations of silicon detectors we take into account the energy loss in detector dead layers and in the carbon foil using the stopping power tables found in the *Stopping and Range of Ions in Matter* (SRIM) catalogue [21]. For example, a proton with an initial energy of $1773\,keV$ loses 2–$3\,keV$ in the carbon foil and 3–$4\,keV$ in the detector dead layer (the variation is due to the varying angle of incidence). The position of the implanted beam is determined from the intensity distribution on the segmented detectors.

2.4 HPGe-detector calibration

The HPGe-detector array is energy calibrated with a ^{152}Eu gamma-ray source. To find the photo-peak centroid we fit the line shape with a Gaussian function. The energy calibration results in an energy resolution of FWHM $= 13.2\,keV$ for the $1408\,keV$ gamma ray in the analog daq and FWHM $= 3.1\,keV$ in the digital daq.

For the absolute efficiency calibration of the total HPGe-detector array we used a ^{152}Eu source with an activity of $A = 16.31(33)\,kBq$ on the day of the measurement and we measured for a total time of $\Delta t = 911(2)$ minutes. The gamma rays used for the calibration ranged
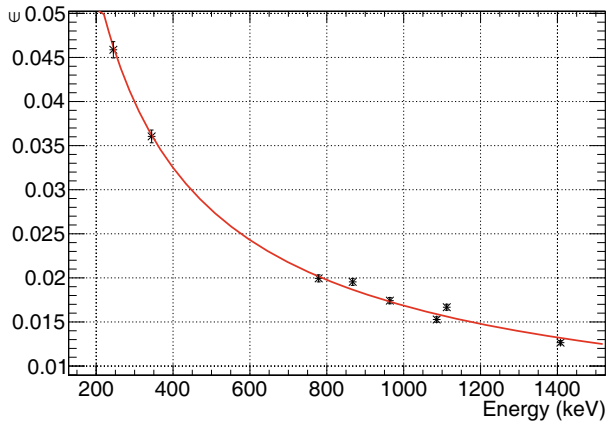
Fig. 2. (Color online) The measured absolute efficiencies with the analog daq and a fit to these data points with the function given in eq. (1).

from 244.6975 keV and up to 1408.006 keV. Gamma-ray energies and intensities have been adopted from ref. [22]. The number of detected gamma rays was determined using a line shape fit of the photo-peak, and translated into absolute efficiencies. The absolute efficiencies determined in this way are described well by the function

$$\epsilon(E) = e^{p_0 + p_1 \cdot \ln(E)}. \tag{1}$$

Fitting the measured efficiencies in the analog daq with this function results in the parameter values $p_0 = 0.869(81)$ and $p_1 = -0.717(12)$ with a covariance term given by $\mathrm{cov}(p_0, p_1) = -0.000988$ (with a reduced χ^2 equal to 3.93). The efficiency function and the measured efficiencies in the analog daq are presented in fig. 2. The effect of summing is small as the total absolute efficiency is low, and as a consequence we do not account for this effect. The observed deviations between the efficiency function and the measured efficiencies, as observed in fig. 2, are mainly caused by the fitting procedure of the photo peaks not being perfect. A similar analysis was performed in the digital daq system, which results in $p_0 = 1.38(8)$ and $p_1 = -0.785(12)$ with a covariance term given by $\mathrm{cov}(p_0, p_1) = -0.00102$ (with a reduced χ^2 equal to 3.34). The final absolute efficiencies as measured with both daq systems are presented in table 1.

3 Analysis

We present the measured proton spectra in sect. 3.1 and compare them with previous measurements from refs. [5, 7]. In sect. 3.2 an updated value for the half-life of ^{20}Mg is presented.

3.1 Spectra

A ΔE-E spectrum showing data from telescope 3 is presented in fig. 3. The events inside the solid (blue) contour are protons that punch through the thin front detector

Table 1. Total absolute gamma-ray efficiency for the HPGe-detector array in percent (the top five efficiencies are from the analog daq, the bottom two efficiencies are from the digital daq).

| E_γ (keV)	$\epsilon(E_\gamma)(\%)$
238.27	4.72(7)
275.09	4.25(6)
983.70	1.705(14)
1232.47	1.451(14)
1297.73	1.398(14)
983.70	1.765(14)
1634.6	1.185(14)
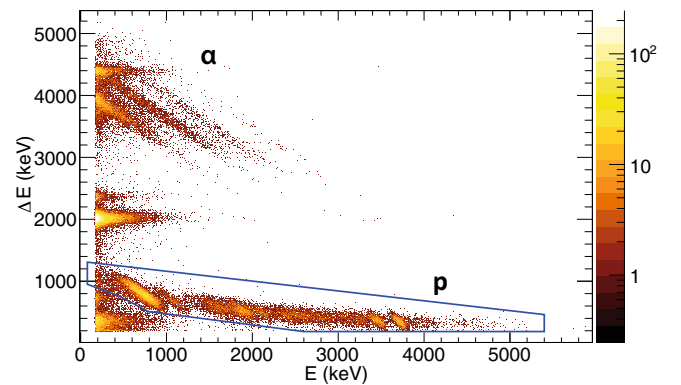
Fig. 3. (Color online) ΔE-E spectrum from the charged-particle telescope consisting of a 20 μm thick SSD front detector and a 500 μm thick DSSSD back detector (telescope no. 3). The events between 3–5 MeV on the vertical axis and 0–2 MeV on the horizontal axis are punch-through alpha particles that reach the back detector. The events inside the solid (blue) line are protons that punch through the front detector. The solid (blue) contour is used as a graphical gate to produce a clean proton spectrum in the back detector, see fig. 4.

and are stopped in the back detector. The main part of the beta-delayed alpha particles from ^{20}Na are stopped in the front detector due to energy losses. However, the highest-energy alpha particles have enough energy to reach the back detector. These alpha particles are the events between 3–5 MeV on the vertical axis and 0–2 MeV on the horizontal axis.

The proton spectrum measured in the back detector of telescope 3 is shown in fig. 4. It exhibits the same features as observed in previous measurements (refs. [5,7]), and we use the same naming convention for the various proton peaks (p_i, where $i = 1, 2, \ldots, 11$). We observe several new proton peaks. We name these with roman numerals from p_I to p_V. More details on the different proton branches contained in the individual proton peaks will be presented in sect. 4.

The low-energy part of the proton spectrum is shown in fig. 5. The data presented here show the events observed in the 40 μm thick DSSSD (telescope no. 4) subjected to three different gates, in order to identify the origin of the
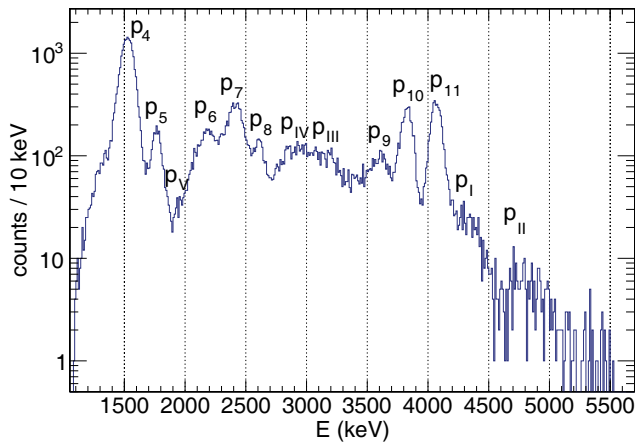
Fig. 4. (Color online) Proton spectrum measured in the $500\,\mu$m thick back detector of telescope no. 3 with an energy resolution of $\sigma = 47$ keV. The spectrum is produced by demanding a multiplicity of 1 in the detector itself, and by only looking at events inside the solid (blue) contour in fig. 3.
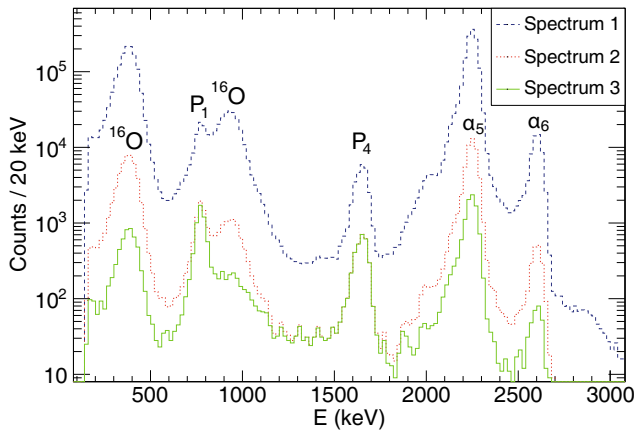
Fig. 5. (Color online) Three different proton spectra with the proton center-of-mass energy as measured in the $40\,\mu$m thick DSSSD in telescope no. 4 with an energy resolution of $\sigma = 20$ keV. Spectrum 1 (dashed blue): the data from the telescope subjected to a graphical gate that cuts away events which punch through the front detector. Spectrum 2 (dotted red): on top of the punch through gate for spectrum 1 we apply a time cut ($t < 100$ ms). Spectrum 3 (solid green): on top of the punch through gate and the time gate we apply the condition that the opposing front detector ($60\,\mu$m DSSSD) measures no particles.

peaks. As the produced beam of ^{20}Mg is strongly contaminated by ^{20}Na, it is important to perform such an identification. Spectrum no. 1 (dashed blue) contains the events observed in the front detector that do not punch through. Spectrum no. 2 (dotted red) is spectrum no. 1 subjected to the additional condition of $t < 100$ ms where t is the time since the last proton pulse on the ISOLDE target. As the half-lives of the two components differ significantly (^{20}Mg has $T_{1/2} = 90(6)$ ms [1] and ^{20}Na has $T_{1/2} = 447.9(2.3)$ ms [1]), such a time gate should reduce the ^{20}Na component relative to the ^{20}Mg component. Spectrum no. 3 (solid green) has the additional con-
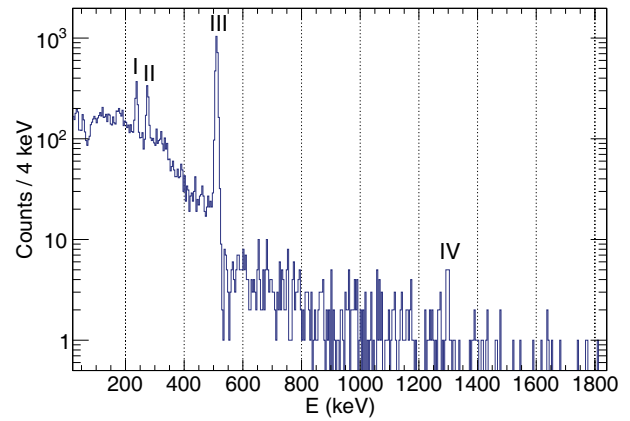

Fig. 6. (Color online) Gamma-ray spectrum from all HPGe detectors in coincidence with the proton spectrum shown in fig. 4. Four gamma-ray peaks are visible: 238 keV (I), 275 keV (II), 511 keV (III) and 1298 keV (IV).

dition that the opposing front detector (telescope no. 1) observes no particles. Considering the kinematics of the decay of ^{20}Na and ^{20}Mg it is clear that only the ^{16}O recoils from ^{20}Na will reach the front detectors. Hence, the effect of applying the last gate will be to reduce the ^{20}Na related peaks in the spectrum while keeping the ^{20}Mg related peaks intact.

The effect of applying the time gate is most clearly observed by focusing on the double peak structure between 600 and 1000 keV. Before applying the time gate the high-energy peak is the most intense, while the time gate reverses the situation. This reflects the fact that the high-energy peak (900–1000 keV) belongs to the decay of ^{20}Na, while the low-energy peak (600–800 keV) belongs to the decay of ^{20}Mg.

The effect of requesting no particle events in the opposing front detector can also be clearly observed in the double peak structure. After having applied the gate, the peak at 600–800 keV belonging to the decay of ^{20}Mg is almost untouched, while the ^{20}Na peak is strongly suppressed. This last gate is therefore a strong tool when identifying the origin of the peaks in the spectrum. It is from the effect of this gate that we conclusively assign the nature of the peaks as highlighted on the figure. We do not observe signs of the previously observed proton branches p_2 and p_3 (notation adopted from refs. [5,7]), due to the large contamination of ^{20}Na.

Figure 6 shows the total gamma-ray spectrum measured in coincidence with the proton spectrum in fig. 4. Three peaks are clearly identified at the energies 238 keV, 275 keV and 511 keV. The 238 keV and 275 keV gamma rays are identified as the de-excitation of the first and second excited states in the proton daughter ^{19}Ne, respectively. The 511 keV gamma ray is caused by annihilation of the emitted β^+-particle. At higher energies we also observe the 1298 keV gamma ray that connects the fourth and first excited states in ^{19}Ne. As expected, we do not observe the 984 keV gamma ray connecting the first excited state and the ground state of ^{20}Na (the state is below the threshold).
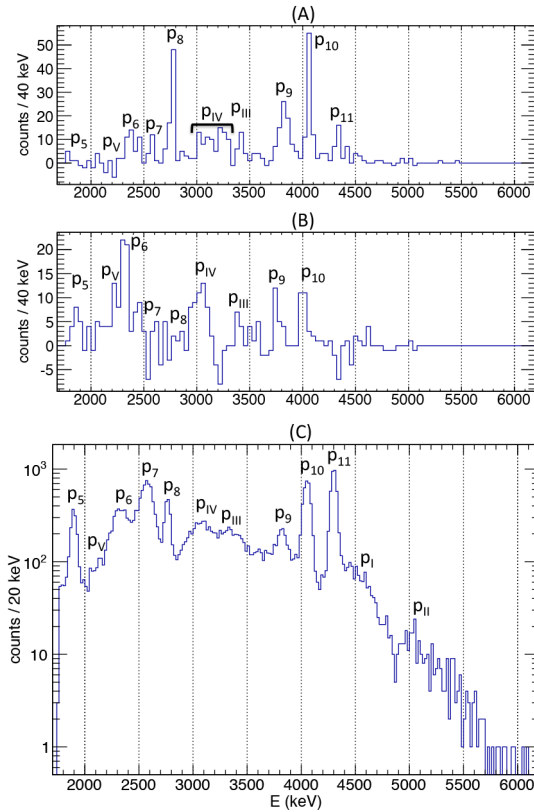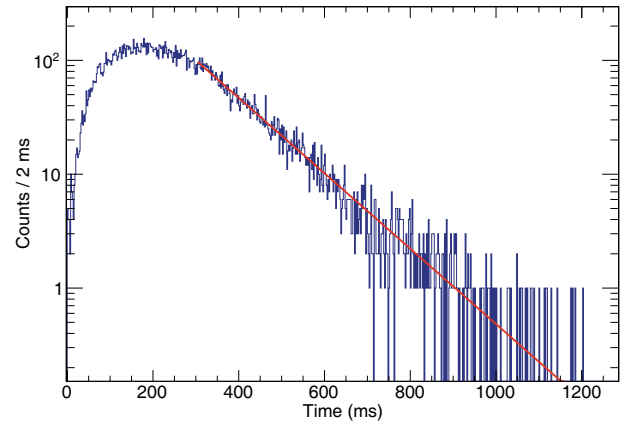
Fig. 7. (Color online) (A) Proton spectrum in the back detector of telescope 4 gated on the 238 keV gamma ray and corrected for background (see text for details). Negative counts are caused by the background subtraction. (B) Proton spectrum in the back detector of telescope 4 gated on the 275 keV gamma ray and corrected for background (see text for details). Negative counts are caused by the background subtraction. (C) Total proton spectrum in the back detector of telescope 4 with an energy resolution of $\sigma = 27$ keV.

The 238 keV and the 275 keV gamma rays are the most intense gamma rays emitted in coincidence with the delayed protons as is evident from fig. 6. Figure 7 shows three different proton spectra as observed in the back detector of telescope 4: (A) in coincidence with the 238 keV gamma ray, (B) in coincidence with the 275 keV gamma ray, (C) proton singles spectrum. Both gamma rays have a background contribution from the Compton continuum of the 511 keV annihilation gamma ray, as is evident from fig. 6. We subtract a background spectrum (with the same energy width as the two gamma-ray gates), in order to obtain the two spectra shown in panels (A) and (B).

3.2 Half-life determination

The half-life of ^{20}Mg was determined from the time distribution of the protons measured with the back detectors of telescope nos. 1, 3 and 4 (telescope no. 2 is not used due to the thick front detector and the resulting contamination from ^{20}Na). As an example, the time distribution from telescope no. 3 is shown in fig. 8. We have fitted the pro-

Fig. 8. (Color online) Half-life fit for the ^{20}Mg decay in the back detector of telescope no. 3 (solid line). The time distribution is from the proton spectrum presented in fig. 4. The fitting is performed on the interval 300–1200 ms with 300 ms being the time when the beam gate was closed allowing the produced ion beam to be transported from the target to the detection chamber (more details can be found in sect. 2.1). The upper limit is 1200 ms which is the time when the next proton pulse possibly arrives at the ISOLDE production target.

ton time distribution from all 3 telescopes with the function $A(t) = \lambda \cdot N_0 \cdot e^{-\lambda \cdot t}$. The fitting is in all three cases performed on the interval 300–1200 ms with 300 ms being the time when the beam gate was closed. The upper limit is 1200 ms which is the time when the next proton pulse possibly arrives at the ISOLDE production target. Using the MINOS error estimation technique from the MINUIT2 minimization package [23] we perform a standard Poisson log-likelihood fit of the data in all three detectors in order to include bins with zero counts and to obtain a more reliable fit when low count numbers are present (≈ 10 or fewer counts per bin). The half-life values determined from the fits are 90.9(1.2) ms with $\chi^2/\text{ndf} = 0.85$ (telescope 3), 90.1(9) ms with $\chi^2/\text{ndf} = 1.05$ (telescope 4) and 96.4(1.7) ms with $\chi^2/\text{ndf} = 0.85$ (telescope 1), which are good fits based on ref. [24]. The three values are not quite consistent, however, making a weighted average value and setting a conservative error we obtain $T_{1/2} = 91.4(1.0)$ ms. This value is to be compared with $T_{1/2} = 90(6)$ ms from the latest evaluation [1]. The two values are in agreement, however, the value measured here is a factor of 6 more precise. Therefore, we use the new value of $T_{1/2}$ when determining the $\log(ft)$-values.

4 Results and discussion

We present an analysis of the content of the individual proton peaks and we perform an extended interpretation of the decay scheme in order to accommodate all the observed proton branches. We also determine the $\log(ft)$-values of the beta decay of ^{20}Mg. We obtain more precise resonance energies in ^{20}Na for a subset of the excited states, and we introduce new excited states. The measured

excitation energy of the IAS is in agreement with a recent gamma-ray de-excitation measurement [8].

4.1 Reconstruction of decay scheme

To reconstruct the decay scheme of ^{20}Mg we have to understand a few essential properties of the data presented in sect. 3.1. Firstly, we need to know the center-of-mass energy of the proton branches. Secondly, we need to understand which decay branches contribute to the different proton peaks, as the energy resolution of the silicon detectors is larger than or comparable to the energy distance between the excited states in ^{19}Ne.

The center-of-mass energy of the different decay branches has been reconstructed by an event-by-event routine, which uses the deposited energy in the detectors as a starting point. The energy reconstruction takes advantage of the detailed knowledge of the geometry of the detector setup from the calibrations, see sect. 2.3. Using the SRIM stopping power tables [21], it is possible to reconstruct the laboratory energy of each event. The conversion to center-of-mass energy is then straightforward, and we do this by assuming that all events are protons.

The center-of-mass energy of the proton peaks have been determined in all the detectors, and a weighted average is constructed. However, in many cases the proton peaks contain several decay branches. In order to determine the energy of the individual proton branches, we look at proton events in coincidence with the 238 keV and the 275 keV gamma rays (see fig. 7(A) and (B)). The number of counts in the produced proton spectra are in general low. This limits the precision of the determination of the proton center-of-mass energy. The center-of-mass energies can be found in table 2.

The next step is to quantify the content of the observed proton peaks, such that we know which decay branches are contained in the individual peaks and how the strength is to be distributed among the various branches. In order to do this we have constructed gamma-ray spectra in coincidence with the individual proton peaks (similar to the coincidence spectrum shown in fig. 6). From these gamma-ray spectra we make a classification of the proton peaks based on the ratio of the efficiency corrected number of gamma rays and the integrated number of protons. We conclude that p_1 only contains a ground-state proton transition. For p_V, p_6, p_8, p_{III}, p_{IV} and p_9 we only observe transitions to excited states. The remaining peaks, except for p_I and p_{II}, contain a mixture of transitions to the ground state and excited states. For p_I and p_{II} we do not obtain any conclusive result —more data are needed.

Finally, we can combine the center-of-mass energies in table 2 with the classification of the proton peaks to reach a decay scheme by assuming that no new states need to be introduced in ^{19}Ne. In order to know which of the excited states in ^{19}Ne are the final state of the proton emission, we use the known gamma-ray de-excitations of the excited states in ^{19}Ne described in sect. 1. In the following we will go through the main ambiguities of the interpretation.

Table 2. Center-of-mass proton energies constructed as an average of the energy measured in the different telescopes. In the first column we specify the proton-peak name along with the final state in ^{19}Ne. In the second column we give the proton energy and in the third column we specify the initial state in ^{20}Na. The proton separation energy in ^{20}Na is $S_p = 2190.1(1.1)$ keV [6]. New proton branches are marked by a $\star$.

Line	E_{cm} (keV)	Initial state (keV)
$p_{1,gs}$	780(8)	2970(8)
$p_{4,gs}$	1656(10)	3846(10)
$p_{4,2nd}$	1622(4)	4094(2)
$p_{5,gs}$	1907(3)	4094(2)
$p_{5,3rd}$	1905(5)	5604(5)
$p_{5,4th}$	1853(40)	5604(5)
$p_{V,3rd}\star$	2120(70)	5836(13)
$p_{6,1st}$	2344(18)	4760(4)
$p_{6,2nd}$	2320(14)	4760(4)
$p_{7,gs}$	2567(4)	4760(4)
$p_{7,3rd}$	2620(14)	6273(7)
$p_{7,4th}$	2560(14)	6273(7)
$p_{8,3rd}$	2830(16)	6496(3)
$p_{8,4th}$	2782(13)	6496(3)
$p_{IV,1st}\star$	3096(17)	5507(10)
$p_{IV,2nd}\star$	3033(12)	5507(10)
$p_{III,1st}\star$	3389(19)	5836(13)
$p_{III,2nd}\star$	3389(18)	5836(13)
$p_{9,1st}$	3820(12)	6273(7)
$p_{9,2nd}$	3782(14)	6273(7)
$p_{10,gs}$	4051(2)	6273(7)
$p_{10,1st}$	4053(12)	6496(3)
$p_{10,2nd}$	4033(12)	6496(3)
$p_{11,gs}$	4303(4)	6496(3)
$p_{11,1st}$	4347(20)	6749(12)
$p_{I,gs}\star$	4544(15)	6749(12)
$p_{II,gs}\star$	4993(16)	7183(16)

The measured proton spectrum in fig. 4 shows clear evidence for destructive interference between p_I and p_{II} (visible as a minimum between the two peaks around 4.6 MeV), which indicates that they populate the same final state in ^{19}Ne. Due to their energy they have to be emitted from resonances above the IAS. Looking for proton coincident gamma rays, we observe inconclusive signs of feeding to excited states in ^{19}Ne. However, we choose the simple interpretation that p_I and p_{II} only contain ground-state transitions. More data are needed to settle the question of components to excited states. This interpretation leads to the introduction of one new resonance at 7183(16) keV in ^{20}Na as the parent of p_{II}. We assign p_I as a ground-state transition from the 6770(100) keV resonance observed in ref. [5]. We also observe the transition
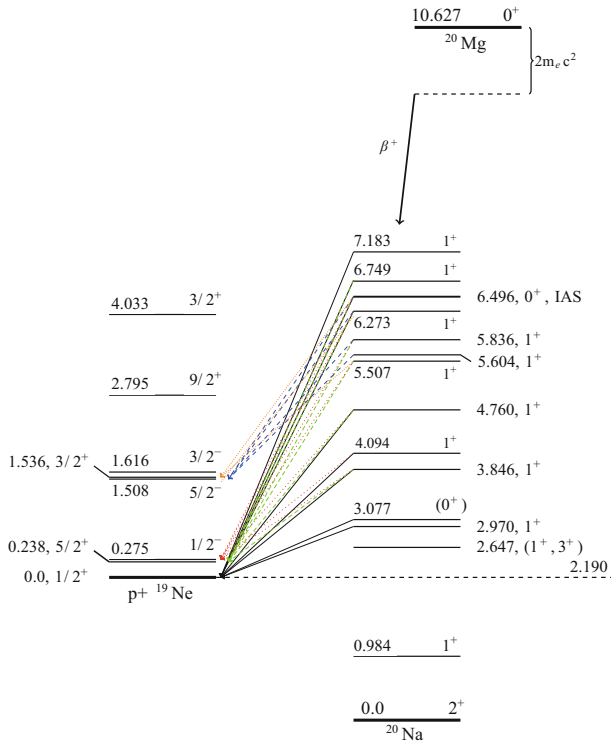
Fig. 9. (Color online) Decay scheme for the ^{20}Mg beta decay, only showing resonances populated in the beta decay. All energies are with respect to the relevant ground state (^{19}Ne and ^{20}Na). The energies of the ^{20}Na resonances are the energies determined in the present study. The different lines (orange dotted, blue dashed, green dashed, red dashed and solid black) correspond to proton decay branches to different final states in ^{19}Ne (4th excited state, 3rd excited state, 2nd excited state, 1st excited state, ground state).

from the 6770(100) keV resonance to the first excited state in ^{19}Ne ($p_{11,1st}$) which is visible in fig. 7(A). The observed beta-delayed proton spectrum shows no evidence for the 6920(100) keV and the 7440(100) keV resonances, which were introduced in ref. [5].

In the energy region between p_8 and p_9 we observe a broad structure visible in fig. 4. Comparing with the proton spectrum in fig. 7, which has a superior energy resolution (27 keV *versus* 47 keV), we observe hints of two broad proton peaks (p_{III} and p_{IV}). However, looking at the proton spectra in coincidence with either the 238 keV or the 275 keV gamma rays, we observe signs of several narrow resonances in the region (see fig. 7). Unfortunately the correct explanation is unclear due to the small number of counts in the coincidence spectra. Therefore, we will make the simplest interpretation, which is the introduction of two new broad resonances in ^{20}Na at 5507(10) keV and 5836(13) keV. The two proton peaks p_{III} and p_{IV} both contain two transitions to the first and second excited state in ^{19}Ne. The new proton peak p_V fits as a transition to the third excited state in ^{19}Ne from the newly introduced 5836(13) keV resonance.

The final reconstruction of the decay scheme can be found in fig. 9 and table 3. The energy levels in ^{19}Ne are

based on the most recent value of the proton separation energy of $S_p(^{20}\text{Na}) = 2190.1(1.1)$ keV from ref. [6]. The most recent measurement of the excitation energy of the IAS in ^{20}Na [8] has moved the energy down by 27 keV to 6498.4(5) keV. We measure the position of the IAS to be at 6496(3) keV, which is in agreement with the updated value found in ref. [8].

4.2 Interference patterns

Allowed Gamow-Teller transitions from the 0^+ ground state of ^{20}Mg will feed 1^+ states in ^{20}Na while the allowed Fermi transition will feed the IAS which is a 0^+ state. As a consequence, the delayed proton spectrum will show signs of interference between protons emitted from the 1^+ states but not with the protons emitted from the IAS. These interference patterns must be consistent with the decay scheme presented in the previous section, where we propose that the following proton peaks contain decay branches emitted by the IAS: p_8, p_{10} and p_{11}. These protons do not show signs of interference effects, which is clear when looking at figs. 4 and 7, as the line shape of the peaks is symmetric. This supports the proposed decay scheme and it is in agreement with the earlier studies [5,7].

The remaining proton peaks are emitted from 1^+ states and are therefore expected to show signs of interference. From fig. 4 it is clear that p_4 and p_7 interfere destructively at the energies between the two peaks, as both appear slightly asymmetric. Both peaks contain intense decay branches to the ground state in ^{19}Ne so the interference is to be expected. The line shape of p_5 appears symmetric with no signs of interference, which can be explained by the low-intensity ground-state transition, see table 5. As p_6 contains decay branches from the 4760(4) keV resonance to the first and second excited states in ^{19}Ne, and the main component of p_7 is the ground-state transition from this state, their line shapes can be understood partly in terms of the 4760(4) keV state being wide.

Looking at fig. 7 we also observe possible signs of interference between p_{IV} and p_{III} as their line shape appears to be slightly asymmetric. This is possibly also the case between p_{III} and p_9. Finally, we also observe a clear interference minimum between p_I and p_{II} as both peaks appear to have an asymmetric line shape. Interference is expected in this case as they both decay to the ground state of ^{19}Ne. All of these observations support the decay scheme presented in the previous section.

4.3 Absolute beta-decay intensities

In order to determine the absolute intensities, we determine the total number of collected ^{20}Mg ions by counting the number of 984 keV gamma rays and the total number of protons observed. The 984 keV gamma ray connects the first excited state with the ground state in ^{20}Na and it is the only decay branch which populates bound states in

Table 3. The ^{20}Na reference energies $E^*(^{20}\mathrm{Na})$ shown in the first column are taken from refs. [5,7–9,25]. In the second column we present the energies determined in this work, which are based on the center-of-mass energies given in table 2. In the remaining columns we present the protons emitted from excited states in ^{20}Na feeding the ground state and excited states in ^{19}Ne. It is important to note that most proton peaks p$_i$ contain several different decay branches and the same p$_i$ are therefore written at several positions below, however, we indicate the final state (f.s.) by the notation p$_{i,\mathrm{f.s.}}$. An example is the 5507(10) keV resonance in ^{20}Na which emits protons to the first and second excited state in ^{19}Ne, and the two branches are named p$_{\mathrm{IV,1st}}$ and p$_{\mathrm{IV,2nd}}$. Three previously unobserved resonances in ^{20}Na have been introduced at 5507(10) keV, 5836(13) keV and 7183(16) keV. The positions of p$_2$ and p$_3$ are based on previous experiments, as they could not have been observed in the present experiment due to ^{20}Na contamination at low energy (see discussion in the text).

$E^*(^{20}\mathrm{Na})$ (keV)		^{19}Ne resonances (MeV, I^π)				
	This work	0.0, 1/2$^+$	0.238, 5/2$^+$	0.275, 1/2$^-$	1.508, 5/2$^-$	1.536, 3/2$^+$
0.0, $T=1$						
984.25(10)						
2647(3)						
2987(2)	2970(8)	p$_{1,\mathrm{gs}}$				
3077(2)		p$_2$				
3871(9)	3846(10)	p$_{4,\mathrm{gs}}$	p$_3$	p$_3$		
4123(16)	4094(2)	p$_{5,\mathrm{gs}}$		p$_{4,\mathrm{2nd}}$		
≈ 4800	4760(4)	p$_{7,\mathrm{gs}}$	p$_{6,\mathrm{1st}}$	p$_{6,\mathrm{2nd}}$		
	5507(10)		p$_{\mathrm{IV,1st}}$	p$_{\mathrm{IV,2nd}}$		
≈ 5600	5604(5)				p$_{5,\mathrm{3rd}}$	p$_{5,\mathrm{4th}}$
	5836(13)		p$_{\mathrm{III,1st}}$	p$_{\mathrm{III,2nd}}$	p$_{\mathrm{V,3rd}}$	
6266(30)	6273(7)	p$_{10,\mathrm{gs}}$	p$_{9,\mathrm{1st}}$	p$_{9,\mathrm{2nd}}$	p$_{7,\mathrm{3rd}}$	p$_{7,\mathrm{4th}}$
6498.4(5), $T=2$	6496(3)	p$_{11,\mathrm{gs}}$	p$_{10,\mathrm{1st}}$	p$_{10,\mathrm{2nd}}$	p$_{8,\mathrm{3rd}}$	p$_{8,\mathrm{4th}}$
≈ 6770	6749(12)	p$_{\mathrm{I,gs}}$	p$_{11,\mathrm{1st}}$			
	7183(16)	p$_{\mathrm{II,gs}}$				

^{20}Na. The branching ratio of the $\beta\gamma$ decay through this state is previously measured to be 69.7(1.2)% [5].

Part of the ions are implanted in a collimator upstream of the detection chamber. As a consequence we observe the gamma rays but not the charged particles emitted by these ions. Therefore, we must determine a correction factor to apply to the number of gamma rays in order to obtain reliable absolute intensities. This is done by looking at the beta decay of ^{20}Na, which has a 79.44(27)% branching ratio for populating the 1634 keV bound state directly [9]. However, due to additional gamma-ray de-excitations of the higher-lying states in ^{20}Ne, the 1634 keV gamma ray will be emitted in 79.88(28)% of the decays [9]. The remaining decays are beta-delayed alpha-particle emission ($I_{\beta\alpha} = 19.95(34)\%$ [9]) and a negligible amount of additional beta-delayed gamma-ray emission. By counting the alpha particles and the number of 1634 keV gamma rays and correcting for dead time and efficiencies, we obtain a branching ratio of 82.4(1.3)% for the emission of the 1634 keV gamma ray.

As a cross-check of the stability of the beam conditions, *i.e.* of the fact that we did implant a constant fraction of the beam in the collimator during the entire experiment, we looked at a subset of the data and determined the branching ratio to be $I_{\beta\gamma}(1634\,\mathrm{keV}) = 82.5(1.3)\%$. This value is consistent with the value determined from the complete data sample, which means that the beam con-

ditions did not change significantly over the course of the experiment.

Using the literature value of $I_{\beta\gamma}^{\mathrm{lit.}}(1634\,\mathrm{keV}) = 79.88(28)\%$ together with the measured number of 1634 keV gamma rays and alpha particles, we construct a scaling factor C_γ to correct for the fraction of the observed gamma rays which are emitted from the collimator. The scaling factor is given by $\frac{C_\gamma A_\gamma}{C_\gamma A_\gamma + A_\alpha} = I_{\beta\gamma}^{\mathrm{lit.}}(1634\,\mathrm{keV})$, where A_γ is the number of 1634 keV gamma rays and A_α is the number of alpha particles observed (both numbers are corrected for efficiency and dead time). We get $C_\gamma = 0.845(22)$, *i.e.* a 15.5% correction for the gamma rays. As a result of the scaling of the number of gamma rays, we may have introduced a systematic uncertainty on the branching ratio. As a conservative estimate we put a 10% relative systematic uncertainty on the branching ratios in general, as 15.5% of the 70% gamma-ray decay branch in ^{20}Mg is 10%. We will not combine this systematic uncertainty with the statistical uncertainties quoted in the rest of the paper.

To determine the number of 984 keV gamma rays measured during the entire experiment, we use the sum of all four clover detectors as recorded by the digital daq. The digital daq system did not suffer from dead time making the extracted number of gamma rays more reliable. From a fit with the gamma-ray line shape function used in the

Table 4. The absolute intensities of the individual proton peaks for the different detectors. Naming convention for the detectors is the detector type followed by the telescope no. according to fig. 1. Remember the 10% relative systematic uncertainty on the intensities, which is not included in the quoted values.

Peak	$I_{\mathrm{abs,i}}^{\mathrm{DSSSD},3}$ (%)	$I_{\mathrm{abs,i}}^{\mathrm{DSSSD},1}$ (%)	$I_{\mathrm{abs,i}}^{\mathrm{DSSSD},4}$ (%)	$I_{\mathrm{abs,i}}^{\mathrm{pad},4}$ (%)	$I_{\mathrm{abs,i}}^{\mathrm{pad},1}$ (%)
p_1		10.9(5)	10.9(4)		
p_4	6.04(18)	7.0(3)	6.3(3)		
p_5	0.66(2)	0.59(6)		0.43(2)	
p_V	0.085(6)			0.109(7)	
p_6	0.41(2)			0.42(3)	
p_7	2.61(8)			2.97(9)	
p_8	0.23(2)			0.87(3)	
p_{IV}	0.94(3)			1.23(4)	
p_{III}	1.00(4)			0.90(3)	
p_9	0.59(2)			0.55(2)	0.89(3)
p_{10}	1.13(4)			1.15(4)	1.24(4)
p_{11}	1.26(4)			1.24(4)	1.33(5)
p_I	0.175(9)			0.343(14)	0.299(13)
p_{II}	0.083(6)			0.102(6)	0.062(5)

efficiency calculation, we deduce that $1.149(6) \cdot 10^5$ gamma rays in the 984 keV photo-peak were observed. Correcting for the efficiency in table 1 and C_γ we get that a total of $5.50(15) \cdot 10^6$ ^{20}Mg nuclei decayed through this channel.

To determine the total number of beta-delayed protons observed during the experiment, we use the $60\,\mu$m front detector of telescope 1 and the $500\,\mu$m back detector of telescope 4 (we observe consistent relative proton intensities when comparing the different detectors with each other). In the back detector we use the total number of events above p_5 (counting from the minimum between p_5 and p_6) and we correct for dead time (8.1%) and solid-angle coverage (4.69(10)%). In the front detector we integrate the counts in the proton peaks p_1, p_4 and p_5 and subtract an estimated background. Finally, we correct for dead time (9.3%) and solid-angle coverage (5.19(12)%) in the front detector. The total number of proton events observed with this method is $2.14(5) \cdot 10^6$.

The total number of ^{20}Mg ions implanted into the setup thus becomes $7.64(16) \cdot 10^6$. With this number we get $I_\beta(984\,\mathrm{keV}) = 72.0(2.5)\%$ with the remaining intensity going into the βp decay mode. This branching ratio has previously been measured to be 69.7(1.2)% by ref. [5], which agrees with the value obtained in the present work.

The absolute proton intensities for the proton peaks can now be determined from the number of events in the proton peak by correcting for the detector solid-angle coverage, the dead time (8.1% for the pad detectors and 9.3% for the DSSSDs) and for the total number of ^{20}Mg ions collected. However, for the front detectors of telescope 1 and 4 we have applied time gates ($t < 100\,\mathrm{ms}$) to the data, which cut away a fraction of the ^{20}Mg events. To correct for this we investigated the ^{20}Mg time distribution shown in fig. 8 and determined the fraction of events occurring during the first 100 ms to be $R = 0.122(2)$. The obtained absolute intensities can be seen in table 4.

When comparing the absolute intensities as measured with the different detectors, we generally have agreement

within two standard deviations. However, several exceptions exist when comparing $I_{\mathrm{abs,i}}^{\mathrm{DSSSD},3}$ with the other detectors. In most cases we observe lower intensities in this detector, which we can explain with a too large background subtraction due to a poor energy resolution of the detector ($\sigma = 47\,\mathrm{keV}$). Therefore we will not use the value of the absolute intensity measured in this detector for any of the proton peaks.

Having determined the absolute intensity of the individual proton peaks, the next step is to quantify how the intensity in the individual peaks is distributed among the final states in ^{19}Ne. Gating on the proton peaks, we look at the coincident gamma-ray spectrum and determine the efficiency corrected number of 238 keV and 275 keV gamma rays. From the ratio of the number of gamma rays to the number of protons, we get the absolute intensity of the individual decay branches in the proton peaks and the result can be seen in table 5.

In table 6 we present the measured absolute beta-decay intensity to the various levels in ^{20}Na on the basis of the decay scheme shown in fig. 9 and the absolute intensities in table 5. The values for I_β presented in the table are the weighted average of the values measured in the different detectors except the back detector of telescope 3. They are compared with the result of ref. [5]. The two experiments in general give consistent results. However, as a consequence of the introduction of the two new resonances at 5507(10) keV and 5836(13) keV, we observe a significant discrepancy in the beta-decay feeding of the 5604(5) keV resonance. For the IAS we measure a significantly lower beta-decay feeding than previously reported. Also, for several resonances we measure an absolute value of I_β where the work presented in ref. [5] only put lower limits. Finally, it should be noted that we obtain a significant improvement in the knowledge of the beta-decay strength distribution above the IAS, as we put an absolute value on I_β for the 6749(12) keV resonance and we introduce the 7183(16) keV resonance. Also we do not

Table 5. Absolute beta-delayed proton emission branching ratios determined as the weighted average of all detectors except the back detector of telescope 3. In a few cases we used a standard average value instead of the weighted average, and we estimated a value for the uncertainty due to inconsistency when comparing the intensities measured in the different detectors. These are marked with a $\star$. Remember the 10% relative systematic uncertainty on the branching ratios, which is not included in the quoted values.

$E^*(^{20}$Na$)$ (keV)		^{19}Ne resonances (MeV, I^π)				
	This work	0.0, 1/2$^+$	0.238, 5/2$^+$	0.275, 1/2$^-$	1.508, 5/2$^-$	1.536, 3/2$^+$
0.0, $T = 1$						
984.25(10)						
2647(3)						
2987(2)	2970(8)	10.9(3)				
3077(2)	p$_2$					
3871(9)	3846(10)	4.8(4)	p$_3$	p$_3$		
4123(16)	4094(2)	0.28(5)		1.9(3)		
≈ 4800	4760(4)	2.3(2)	0.31(8)	0.7(1)		
	5507(10)		0.54(8)	0.46(8)		
≈ 5600	5604(5)				0.13(4)	0.03(2)
	5836(13)		0.37(6)	0.08(2)	0.109(7)	
6266(30)	6273(7)	0.7(3)$\star$	0.44(5)	0.24(15)$\star$	0.4(2)	0.33(9)
6498.4(5), $T = 2$	6496(3)	0.97(9)	0.3(2)$\star$	0.31(7)	0.10(3)	0.47(7)
≈ 6770	6749(12)	0.319(10)	0.27(8)			
	7183(16)	0.08(3)$\star$				

Table 6. Absolute beta-decay branching ratios and log(ft)-values for the individual resonances in ^{20}Na determined as the weighted average of all detectors except the back detector of telescope 3. The present work is compared with ref. [5]. Note that the absolute intensities of p$_2$ and p$_3$ are not included here. The resonance energies in ^{20}Na are the value measured in the present experiment. However, the resonances marked with a $\star$ are not observed here and the energy quoted are from ref. [5]. The uncertainty on the log(ft)-values only comes from I_β as it dominates. Remember the 10% relative systematic uncertainty on the branching ratios. These are not included in the quoted uncertainty values.

$E^*(^{20}$Na$)$ (keV)	I_β (%)		log(ft)	
This work	This work	Ref. [5]	This work	Ref. [5]
984.10(25)	72.0(2.5)	69.7(1.2)	3.78(3)	3.83(2)
2970(8)	10.9(3)	11.5(1.4)	4.07(3)	4.08(6)
3846(10)	4.8(4)	4.8(6)	4.25(8)	4.17(6)
4094(2)	2.2(3)	2.7(3)	4.50(14)	4.33(6)
4760(4)	3.3(3)	≥ 1.9	4.06(9)	≤ 4.23
5507(10)	1.00(11)		4.25(11)	
5604(5)	0.16(4)	≥ 1.5	5.0(3)	≤ 3.97
5836(13)	0.56(7)		4.34(13)	
6273(7)	2.1(4)	1.2(1)	3.5(2)	3.72(6)
6496(3), $T = 2$	2.2(2)	3.3(4)	3.36(9)	3.13(6)
6749(12)	0.59(8)	≥ 0.03	3.77(14)	≤ 5.01
6920(100)*		≥ 0.01		≤ 5.39
7183(16)	0.08(3)		4.3(4)	
7440(100)*		≥ 0.01		≤ 4.99

observe signs of the previously proposed 6920(100) keV and 7440(100) keV resonances [5].

The total branching ratio for beta-delayed proton emission is measured to be 27.7(8)% (p$_2$ and p$_3$ not included) where we need to remember the 10% relative systematic uncertainty, which gives a total relative uncertainty of 10.4%. This value is to be compared with the 26.9(3.2)% from ref. [5]. The two values are consistent.

The log(ft)-values quoted in table 6 are calculated with the parametrization of the phase space factor given in ref. [26]. We use the measured value of the half-life presented in sect. 3.2, $T_{1/2} = 91.4(1.0)$ ms, and the recently reported measurement of the Q-value in ref. [8], $Q_{EC} = 10627.1(2.3)$ keV, as input parameters. For the resonance energies we use the values measured in the present experiment presented in table 6. The determined log(ft)-values are in general consistent with the values given in ref. [5]. In the case of the 5604(5) keV resonance we disagree significantly with [5]. However, this inconsistency can be explained by the introduction of the two new resonances in ^{20}Na at 5507(10) keV and 5836(13) keV.

On the basis of the measured log(ft)-value of the IAS, log(ft) = 3.36(9), we determine the Fermi beta-decay strength to be $B_F = 2.7^{+0.6}_{-0.5}$ (not including the 10% relative systematic uncertainty on I_β(IAS)). This is to be compared with the sum rule expectation given by $\sum B_F^+ - \sum B_F^- = Z - N = 4$. The measured value is low compared to the sum rule expectation, which may be caused by unobserved strength to the IAS in the form of decay branches with an absolute intensity of about 1%. Possible unobserved decay modes could be alpha-particle emission and gamma-ray emission. We have not observed signs of any alpha particles from the decay of ^{20}Mg, however, these would be very difficult to identify considering the amount of alpha particles observed from the decay of ^{20}Na. Based on calculations made in an sd shell model [8], it is expected that the main gamma decay of the IAS populates the 984 keV bound state. This branch is expected to be an order of magnitude more intense than any other gamma-ray decay branch from the IAS. By studying the observed gamma rays in the digital daq, we estimate that $I_{\beta\gamma}$(IAS → 984 keV) < 0.7% with 95% confidence (the absolute gamma-ray efficiency value used is based on eq. (1)). It means that the missing beta-decay strength to the IAS could accomodate other decay modes than gamma-ray decays.

The mirror asymmetry parameter $\delta = (ft)^+/(ft)^- - 1$ can be computed for the mirror transitions ^{20}O → ^{20}F(3488 keV) and ^{20}Mg → ^{20}Na(2987 keV). Using log(ft)$^-$ = 3.65(6) from ref. [27], we obtain a value of $\delta = 1.6(4)$, which is consistent with the value obtained in ref. [5].

4.4 Feeding of the 2647(3) keV resonance in ^{20}Na

The resonance at 2647(3) keV in ^{20}Na is located in the Gamow window of the ^{19}Ne(p, γ)^{20}Na reaction as discussed in sect. 1. Its spin and parity can be either 1$^+$ or 3$^+$, with the value of 3$^+$ being favored on the basis of

the latest result, $I_{\beta p} < 0.02\%$ [7]. A 3$^+$ assignment is expected to lead to a significantly higher reaction rate than a 1$^+$ assignment according to refs. [7,28]. The resonance decays either by proton emission to the ground state of ^{19}Ne with $E_{cm} = 456$ keV (b.r. ≈ 90% [29]) or by gamma-ray de-excitation. The 2647(3) keV resonance will, according to ref. [29], decay by emission of a 1847(6) keV gamma ray to the 4$^+$ state at 798.56(6) keV when assuming a 3$^+$ assignment. However, assuming a 1$^+$ assignment for the resonance, it will decay by emission of a 1613(6) keV gamma ray to the 1$^-$ state at 1031.9(7) keV [29].

A search for the beta-delayed proton branch from this resonance is difficult with the available data, due to the large background at low energies from the decay of ^{20}Na —this is clear when looking at fig. 5 where the ^{16}O recoils makes it impossible to determine an improved value on the branching ratio limit. Instead we investigate whether we have observed any signs of feeding in the gamma-ray spectrum. Based on the number of collected ^{20}Mg ions, the present upper limit of $I_{\beta p}$(2647 keV) < 0.02% and the expected branching ratio of roughly 10% [29], we estimate that fewer than 160 gamma-ray decays, in either I^π-scenarios, occurred during the experiment. Considering that the total absolute efficiency of the HPGe-detector array at the relevant energy is roughly 1%, we expect to observe a total of approximately 1–2 counts with the combined HPGe-detector array. It is therefore not feasible to observe feeding of the 2647(3) keV resonance with gamma-ray data available.

4.5 Search for beta-delayed proton decays to the 4032.9(2.4) keV resonance in ^{19}Ne

The 4032.9(2.4) keV resonance in ^{19}Ne is located in the Gamow window of the ^{15}O(α, γ)^{19}Ne reaction, and it can be fed by beta-delayed proton emission from ^{20}Mg. As discussed in sect. 1, it is important to measure directly the branching ratio for alpha-particle emission from this resonance, which is expected to be roughly 10^{-4} [13,14]. However, the 4032.9(2.4) keV resonance will mainly decay by emission of a 4.03 MeV gamma ray to the ground state. As gamma-ray emission is much more likely than alpha-particle emission, it makes sense first to establish feeding of the 4032.9(2.4) keV resonance by detecting the 4.03 MeV gamma ray. Then we can search for the alpha-particle emission if it is feasible.

The total gamma-ray spectrum as measured with the digital daq is shown in fig. 10, and it shows no sign of the 4.03 MeV gamma ray. However, we can estimate an upper limit on the feeding of the resonance by modeling the line shape of the photo-peak from a 4.03 MeV gamma ray. Using the same line shape function as used in the efficiency calibration, we estimate the Gaussian width σ by fitting the 3333 keV gamma ray from the decay of ^{20}Na, and we estimate a +3 keV systematic offset on the centroid from this fit. Then we fit the spectrum close to 4 MeV with a linear function to describe the background contribution. Using the obtained parameters, we
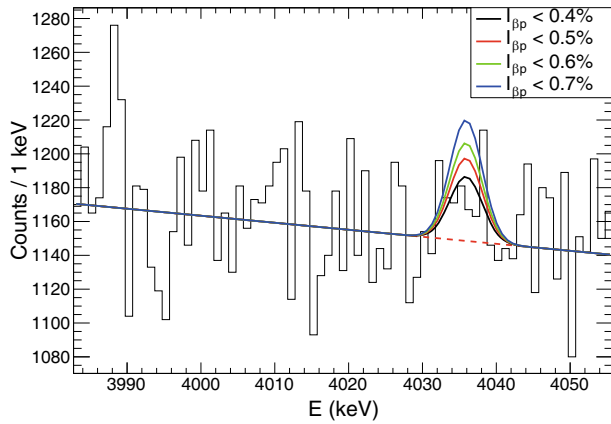
Fig. 10. (Color online) Total gamma-ray spectrum around 4 MeV as observed in the digital daq. Based on the line shapes drawn in the figure (solid lines with different colors) with varying intensities ($I_{\beta p}$), we estimate an upper limit of the beta-decay feeding of the 4032.9(2.4) keV resonance.

can then model the 4.03 MeV gamma-ray photo-peak assuming various number of events in the peak. The number of events is translated to an intensity through the total absolute gamma-ray efficiency $\epsilon(4.03\,\mathrm{MeV}) = 0.587(13)\%$ (the value is based on eq. (1)), the scaling factor C_γ and the total number of collected ^{20}Mg ions $(7.64(16) \cdot 10^6)$. The final upper limit is estimated to be $I_{\beta p} < 0.7\%$ with a 68% confidence level. Assuming that the branching ratio for alpha-particle emission is 10^{-4}, this upper limit corresponds to roughly 5 alpha particles being emitted from the 4032.9(2.4) keV resonance during the experiment. However, considering the amount of beta-decay strength identified as going to the resonances above the IAS in ^{20}Na ($I_\beta = 0.67(9)\%$), we expect a somewhat lower feeding of the 4032.9(2.4) keV resonance. As a consequence it is not feasible to search for the emitted alpha particle with the present data.

A search focused on identifying beta-delayed proton branches feeding the 4032.9(2.4) keV resonance is strongly hindered by their expected center-of-mass energies for the IAS and the two levels above it: 273 keV (IAS), 526 keV (6749 keV) and 960 keV (7183 keV). The low-energy proton spectrum was presented in fig. 5, and it has a large background component from ^{16}O.

5 Summary and conclusions

Beta-delayed proton emission has been measured at the ISOLDE facility with a close geometry silicon detector array including angular resolution and high efficiency, and surrounded by an array of four HPGe clover detectors. Several results have been extracted from the observed proton and gamma-ray spectra:

– The half-life of ^{20}Mg has been measured to be $T_{1/2} = 91.4(1.0)$ ms, which improves on the previous value of 90(6) ms [1].

– Seven new beta-delayed proton branches have been observed out of 27 beta-delayed proton branches in total. The delayed proton spectrum covers energies between 0.8 and 5.0 MeV.

– Three new resonances have been introduced above the proton separation energy in ^{20}Na: 5507(10) keV, 5836(13) keV and 7183(16) keV.

– The measured resonance energy of the IAS, 6496(3) keV, agrees well with the recent measurement in ref. [8] of 6498.4(5) keV. Hence we confirm the recent revalidation of the IMME for the $A = 20$ quintet, which follows from this result.

– More precise energies have been obtained for the 4760(4) keV, 5604(5) keV and 6749(12) keV resonances.

– The Fermi strength to the IAS has been measured to be $B_F = 2.7^{+0.6}_{-0.5}$ (not including the 10% systematic uncertainty) which is lower than the sum rule prediction ($B_F = 4$).

– Absolute beta-decay intensities have been measured for the first time for the 4760(4) keV, 5604(5) keV and 6749(12) keV resonances.

– We have observed feeding to two resonances above the IAS, which makes it possible for beta-delayed proton emission to feed the 4032.9(2.4) keV resonance in ^{19}Ne. The resonance is important for determining the ^{15}O(α, γ)^{19}Ne reaction rate. However, at the present level of sensitivity we see no sign of feeding to the 4032.9(2.4) keV state ($I_{\beta p} < 0.7\%$ with 68% confidence).

– No sign is observed of feeding of the 2647(3) keV resonance, which is relevant for the ^{19}Ne(p, γ)^{20}Na reaction rate.

– No evidence is observed for the previously proposed 6920(100) keV and 7440(100) keV resonances.

Based on these findings an updated decay scheme for ^{20}Mg has been presented in fig. 9 and in table 3.

References

1. G. Audi *et al.*, Chin. Phys. C **36**, 1157 (2012).
2. B. Blank, M.J.G. Borge, Prog. Part. Nucl. Phys. **60**, 403 (2008).
3. M. Pfützner, L.V. Grigorenko, M. Karny, K. Riisager, Rev. Mod. Phys. **84**, 567 (2012).
4. M.J.G. Borge, Phys. Scr. **T152**, 014013 (2013).

5. A. Piechaczek, M.F. Mothar, R. Anne, V. Borrel, B.A. Brown, J.M. Corre, D. Guillemaud-Mueller, R. Hue, H. Keller, S. Kubono, V. Kunze, M. Lewitowicz, P. Magnus, A.C. Mueller, T. Nakamura, M. Pfützner, E. Roeckl, K. Rykaczewski, M.G. Saint-Laurent, W.-D. Schmidt-Ott, O. Sorlin, Nucl. Phys. A **584**, 509 (1995).

6. C. Wrede, J.A. Clark, C.M. Deibel, T. Faestermann, R. Hertenberger, A. Parikh, H.-F. Wirth, S. Bishop, A.A. Chen, K. Eppinger, A. Garcia, R. Krücken, O. Lepyoshkina, G. Rugel, K. Setoodehnia, Phys. Rev. C **81**, 055503 (2010).

7. J.P. Wallace, P.J. Woods, G. Lotay, A. Alharbi, A. Banu, H.M. David, T. Davinson, M. McCleskey, B.T. Roeder, E. Simmons, A. Spiridon, L. Trache, R.E. Tribble, Phys. Lett. B **712**, 59 (2012).

8. B.E. Glassman, D. Pérez-Loureiro, C. Wrede, J. Allen, D.W. Bardayan, M.B. Bennett, B.A. Brown, K.A. Chipps, M. Febbraro, C. Fry, M.R. Hall, O. Hall, S.N. Liddick, P. O'Malley, W. Ong, S.D. Pain, S.B. Schwartz, P. Shidling, H. Sims, P. Thompson, H. Zhang, Phys. Rev. C **92**, 042501 (2015).

9. N.T.H. Clifford, E. Hagberg, J.C. Hardy, H. Schmeing, R.E. Azuma, H.C. Evans, V.T. Koslowsky, U.J. Schrewe, K.S. Sharma, I.S. Towner, Nucl. Phys. A **493**, 293 (1989).

10. D.R. Tilley, H.R. Weller, C.M. Cheves, R.M. Chasteler, Nucl. Phys. A **595**, 1 (1995).

11. C. Illiadis, *Nuclear Physics of Stars* (Wiley-VCH, Weinheim, 2007).

12. B. Davids, R.H. Cyburt, J. José, S. Mythili, Astrophys. J. **735**, 40 (2011).

13. C. Wrede, PoS **NIC XIII**, 039 (2014).

14. W.P. Tan, J.L. Fisker, J. Görres, M. Couder, M. Wiescher, Phys. Rev. Lett. **98**, 242503 (2007).

15. M.V. Lund, PhD Thesis (Aarhus University, Denmark, 2016) http://cds.cern.ch/record/2153139.

16. E. Kugler, Hyperfine Interact. **129**, 23 (2000).

17. V.N. Fedoseyev, G. Huber, U. Köster, J. Lettry, V.I. Mishin, H. Ravn, V. Sebastian, Hyperfine Interact. **129**, 409 (2000).

18. Richard G. Sextro, R.A. Gough, Joseph Cerny, Phys. Rev. C **8**, 258 (1973).

19. M.V. Lund, M.J.G. Borge, J.A. Briz, J. Cederkäll, H.O.U. Fynbo, J.H. Jensen, B. Jonson, K.L. Laursen, T. Nilsson, A. Perea, V. Pesudo, K. Riisager, O. Tengblad, Phys. Lett. B **750**, 356 (2015).

20. M.V. Lund, M.J.G. Borge, J.A. Briz, J. Cederkäll, H.O.U. Fynbo, J.H. Jensen, B. Jonson, K.L. Laursen, T. Nilsson, A. Perea, V. Pesudo, K. Riisager, O. Tengblad, Eur. Phys. J. A **51**, 113 (2015).

21. J.F. Ziegler, J.P. Biersack, M.D. Ziegler, *SRIM - The Stopping and Range of Ions in Matter*, 5th ed. (SRIM Co., USA, 2008).

22. The Lund/LBNL Nuclear Data Search, *WWW Table of Radioactive Isotopes*, Version 2.0, February 1999.

23. F. James, M. Winkler, *Minuit User's Guide* (CERN, Geneva, 2004).

24. U.C. Bergmann, K. Riisager, Nucl. Phys. A **701**, 213c (2002).

25. J.P. Wallace, P.J. Woods, Phys. Rev. C **86**, 068801 (2012).

26. D.H. Wilkinson, B.E.F. Macefield, Nucl. Phys. A **232**, 58 (1974).

27. D.E. Alburger, G. Wang, E.K. Warburton, Phys. Rev. C **35**, 1479 (1987).

28. H.T. Fortune, R. Sherr, B.A. Brown, Phys. Rev. C **61**, 057303 (2000).

29. D. Seweryniak, P.J. Woods, B. Blank, M.P. Carpenter, T. Davinson, S.J. Freeman, J. Görres, A. Heinz, R.V.F. Janssens, H. Mahmud, T.L. Khoo, Z. Liu, G. Mukherjee, E. Rehm, F. Sarazin, J. Shergur, M. Shawcross, S. Sinha, A. Woehr, Phys. Lett. B **590**, 170 (2004).